

Uniform Luminous Perovskite Nanofibers with Color-Tunability and Improved Stability Prepared by One-Step Core/Shell Electrospinning

Ping-Chun Tsai, Jung-Yao Chen, Ender Ercan, Chu-Chen Chueh, Shih-Huang Tung,* and Wen-Chang Chen*

A one-step core/shell electrospinning technique is exploited to fabricate uniform luminous perovskite-based nanofibers, wherein the perovskite and the polymer are respectively employed in the core and the outer shell. Such a coaxial electrospinning technique enables the in situ formation of perovskite nanocrystals, exempting the needs of presynthesis of perovskite quantum dots or post-treatments. It is demonstrated that not only the luminous electrospun nanofibers can possess color-tunability by simply tuning the perovskite composition, but also the grain size of the formed perovskite nanocrystals is largely affected by the perovskite precursor stoichiometry and the polymer solution concentration. Consequently, the optimized perovskite electrospun nanofiber yields a high photoluminescence quantum yield of 30.9%, significantly surpassing the value of its thin-film counterpart. Moreover, owing to the hydrophobic characteristic of shell polymer, the prepared perovskite nanofiber is endowed with a high resistance to air and water. Its photoluminescence intensity remains constant while stored under ambient environment with a relative humidity of 85% over a month and retains intensity higher than 50% of its initial intensity while immersed in water for 48 h. More intriguingly, a white light-emitting perovskite-based nanofiber is successfully fabricated by pairing the orange light-emitting compositional perovskite with a blue light-emitting conjugated polymer.

full width at half maximum (FWHM), and the composition-dependent tunable light emission. Such appealing features have enabled this emerging class of materials to be applied in the light-emitting diodes, light-emitting transistors, photomemories, and nanolasers in addition to the light-harvesting related applications.^[1–10] Furthermore, the perovskite materials are also competitive for the applications in memory devices, radiation and chemical sensors, and energy generators due to their exceptional electrical properties.^[10]

Accompanied with the rapid development of bulk perovskite, the colloidal perovskite nanocrystals have also drawn numerous research interests.^[11–13] It was reported that the energy spectrum of an emissive compound became discrete as its dimension was reduced to nanoscale (tens nanometer). Consequently, not only the resulting bandgap was size-dependent but also the photoluminescence (PL) would be blue-shifted and intensified with the decrease of the nanocrystal's size, known as the quantum confinement.^[13–18]

Thus far, versatile methods have been

1. Introduction

Recently, the organic–inorganic hybrid perovskite materials have attracted worldwide attention in the light-emitting applications due to their low-cost and facile preparations, high photoluminescence quantum yield (PLQY) associated with narrow

explored to modulate the nanostructure of perovskite materials, especially by means of controlling the stoichiometry of the perovskite precursors. To this end, both the crystal size/structure and the luminescence properties of perovskite materials can be effectively regulated. For instance, Yan et al.^[19] and Lee et al.^[20] respectively manifested that tuning the CH_3NH_3^+ abundant environment was a straightforward strategy to modulate the crystal formation of perovskite films, thus leading to an intensified PL. On the other hand, Zhang et al.^[21] revealed that a ligand-assisted reprecipitation technique, wherein the *n*-octylamine and oleic acid were added into the perovskite precursor solution as surfactants, can enhance the PL intensity and PLQY (to 70%) of $\text{CH}_3\text{NH}_3\text{PbBr}_3$. Very recently, Kaltenbrunner et al.^[18] employed nanoporous alumina or silicon as a scaffold to regulate the shape/size of the nanocrystalline perovskite (less than 10 nm) to exhibit conspicuous quantum size effects. Despite such achievements, the researchers are still seeking a facile method exempting from tedious purification or post-treatment to prepare the perovskite materials, which is

P.-C. Tsai, Prof. S.-H. Tung, Prof. W.-C. Chen
Institute of Polymer Science and Engineering
National Taiwan University
Taipei 10617, Taiwan

E-mail: shtung@ntu.edu.tw; chenwc@ntu.edu.tw

Dr. J.-Y. Chen, E. Ercan, Prof. C.-C. Chueh, Prof. W.-C. Chen
Department of Chemical Engineering
National Taiwan University
Taipei 10617, Taiwan

 The ORCID identification number(s) for the author(s) of this article can be found under <https://doi.org/10.1002/sml.201704379>.

DOI: 10.1002/sml.201704379

beneficial for the widespread applications of perovskite materials in the optoelectronic devices.

Besides the typical thin-film preparation, electrospinning technique has recently attracted great attention and been considered as a powerful tool to prepare nanocrystalline fibers. It has been proven as a simple, high throughput process for preparing polymeric nanofibers with enhanced crystallinity.^[22–25] Moreover, the electrospun nanofibers could serve as an effective matrix for the functional materials such as metallic nanoparticles, conjugated polymers, and quantum dots to prepare composite fibers for diverse device applications.^[26–32] It was reported that the synthesized perovskite quantum dots were incorporated into the electrospun fibers to mitigate its aggregation issue while maintaining its pristine optical properties.^[33–35] Another important advantage of electrospun fiber lies in its implanted geometrical confinement effect, which can manipulate the orientation, crystallinity, and optoelectronic properties of the components embedded in the nanofibers.^[36,37] For example, Kuo et al.^[26] unveiled that the aggregates of polyfluorene in the nanofibers were much smaller than those in the spin-cast counterpart due to the geometrical confinement effect, which resulted in a blue-shifted emission along with improved PLQY. Meanwhile, the crystal size and orientation of Ag nanoparticles (NPs) in the composite Ag/poly(vinyl pyrrolidone) electrospun nanofibers have also been demonstrated to closely correlate with the concentration of the shell polymer.^[23] Based on these inspiring findings, we herein are interested to exploit the perovskite-based electrospun nanofibers and investigate the ensuing geometric confinement effects as considering it has not been widely explored yet in the literature.

In this study, we successfully prepared uniform luminous perovskite electrospun nanofibers through one-step coaxial electrospinning method, wherein the perovskite materials and polyacrylonitrile (PAN) were used as the core and shell precursors, respectively. PAN is selected as the shell material because of its semicrystalline and hydrophobic characteristics that satisfy the purpose of protecting the perovskites from moisture. We revealed that the morphology of perovskite nanocrystals inside the prepared fibers as well as the resultant photophysical properties could be effectively manipulated through tuning the perovskite precursor composition and stoichiometry, shell polymer concentration, and solvent additives. As a result, the composite perovskite/PAN electrospun nanofibers prepared through such coaxial electrospinning technique possessed color-tunability and were endowed with high PLQY (up to 30.9%) and a superior water-proof feature. More intriguingly, we further partially blended a blue light-emitting polymer, poly[(9,9-bis(3'-(*N,N*-dimethylamino)propyl)-2,7-fluorene)-alt-2,7-(9,9-dioctylfluorene)] (PFN) into the shell PAN and optimized the halide composition of the core perovskite materials to obtain a white light-emitting perovskite-based nanofibers.

2. Results and Discussion

2.1. Perovskite Light-Emitting Fibers Prepared by Coaxial Electrospinning

Figure 1 shows the schematic of the one-step coaxial electrospinning setup with the precursor solution of methylammonium halides (MAX, X = Cl, Br, I) and PbX_2 at varying ratios in the core and PAN solution in the shell and the detailed compositions of the solutions for different samples are listed in Table 1. Shown in Figure 2a–c are the scanning electron microscopy (SEM) images of the prepared electrospun fibers comprising PAN and compositional perovskites, wherein the used composition of perovskite denotes the sample's name, such as MAPbCl_3 -1, MAPbBr_3 -1, and MAPbI_3 -1, respectively. As seen, all the fabricated fibers are uniform and show average diameters of 400–700 nm. Also, their surfaces are smooth, indicating no perovskite crystals were appeared on the fiber surface.

Their corresponding internal structures were further investigated by transmission electron microscopy (TEM) and shown in Figure 2d–f. Benefitting from the higher electron density of perovskites than polymer, the perovskite crystals can be clearly distinguished from the PAN matrix. As can be clearly seen, all the perovskite crystals are depleted on the surface and well dispersed inside the fibers. It affirms that the shell polymer can provide certain geometric confinement to restrict the distribution of perovskite nanocrystals inside the fibers. For the MAPbCl_3 -1 (Figure 2d) and MAPbBr_3 -1 (Figure 2e) fiber, the shape of the in situ formed perovskite nanocrystals is sphere with an average size of $\approx 41.97 \pm 15.01$ and $\approx 26.89 \pm 6.96$ nm, respectively.^[38,39] Interestingly, instead of spherical crystals, MAPbI_3 nanofibers (Figure 2f) possess rod-like nanocrystals with a diameter ranging from 40 to 80 nm. It has been reported that MAPbI_3 adopts a tetragonal crystal structure while MAPbCl_3 and MAPbBr_3 crystallize in a cubic form, which may be responsible for the different geometry as MAPbI_3 crystal

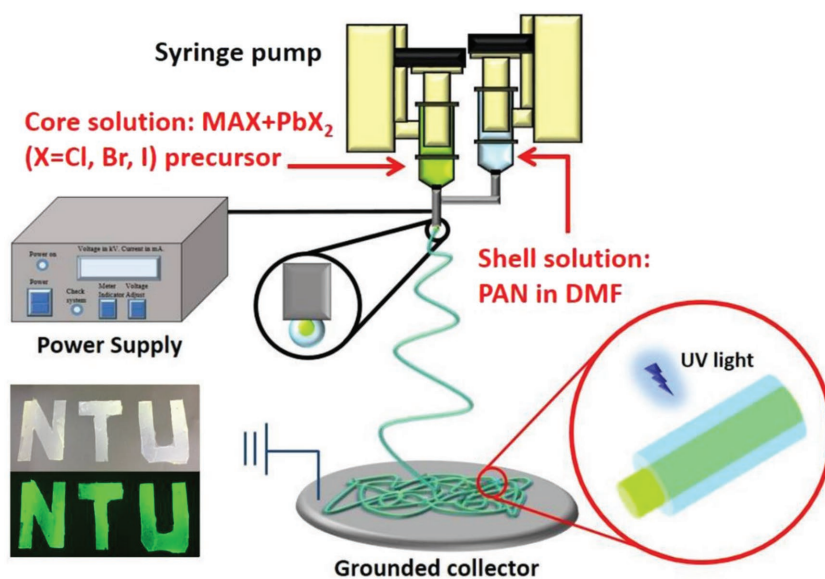


Figure 1. Schematic of the one-step coaxial electrospinning setup to fabricate the core/shell-perovskite light-emitting nanofibers.

Table 1. Preparation conditions and characteristics of the samples.

Samples	MAX: PbX ₂	PAN concentration [mg mL ⁻¹]	Diameter [nm] ^{a)}	PL Peak position [nm]	PLQY [%]	(X,Y)	PL FWHM [nm] ^{b)}	XRD FWHM [degree] ^{c)}
Single-halide perovskites MAPbX ₃ (X = Cl, Br, I)								
MAPbCl ₃ -1	1.5:1	100	551 ± 95	394	1.5	(0.1474, 0.1797)	60.74	0.04
MAPbI ₃ -1	1.5:1	100	709 ± 119	742	1.1	(0.7014, 0.2985)	51.17	0.01
MAPbBr ₃ -1	1.5:1	100	477 ± 65	522	21.9	(0.1575, 0.7442)	27.66	0.14
MAPbBr ₃ -2	3:1	100	541 ± 89	520	24.8	(0.1813, 0.6953)	30.16	0.15
MAPbBr ₃ -3	3:1	60	194 ± 16	510	30.9	(0.0860, 0.6709)	25.68	0.20
MAPbBr ₃ film	3:1	60	NA	539	6.8	(0.2364, 0.6702)	23.65	0.11
Mixed-halide perovskites MAPb(Br _x I _{1-x}) ₃								
X = 0.8	1.5:1	100	NA	550	NA	NA	34.43	NA
X = 0.6	1.5:1	100	NA	589	NA	(0.4594, 0.5173)	39.35	NA
X = 0.4	1.5:1	100	NA	654	NA	NA	58.32	NA
X = 0.2	1.5:1	100	NA	711	NA	NA	56.29	NA

^{a)}Diameter of electrospun nanofiber; ^{b)}the line broadening at half the maximum intensity (FWHM) of PL peak; ^{c)}(According to the Scherrer equation the line broadening at half the maximum intensity (FWHM) inversely proportional to the grain size).

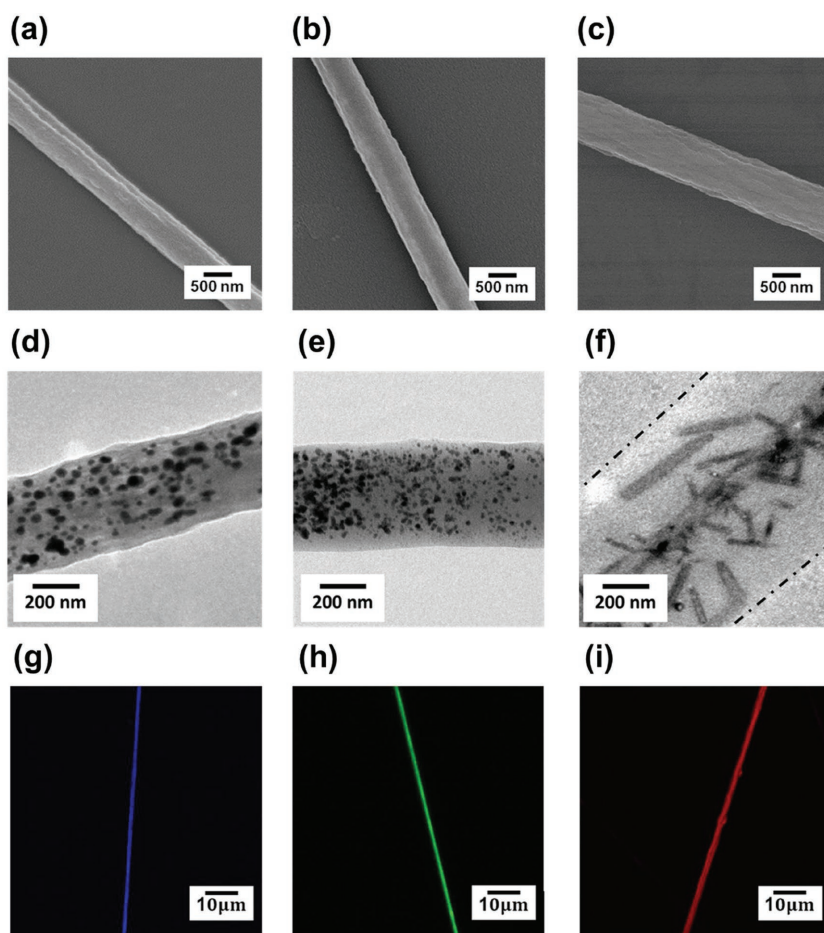


Figure 2. SEM images of a) MAPbCl₃-1, b) MAPbBr₃-1, and c) MAPbI₃-1 fibers. The TEM images of d) MAPbCl₃-1, e) MAPbBr₃-1, and f) MAPbI₃-1 fibers, and the confocal images of g) MAPbCl₃-1, h) MAPbBr₃-1, and i) MAPbI₃-1 fibers.

grows.^[31,40,41] Additionally, the long axes of the nanorods are approximately along the fibers, which can be attributed to the strong stretching force during the electrospinning process that orient the growth direction of perovskite crystals.

It is worthwhile to note that the perovskite crystals of the electrospun fibers prepared by the uniaxial electrospinning method are much larger (173.43 ± 50.56 nm) and poorly distributed inside the fibers as shown in Figure S1a in the Supporting Information, wherein some perovskite crystals are appeared on the fiber surface and directly exposed to air. PAN can chelate perovskite precursors due to the strong interactions between the precursors and the polar group on PAN, which may affect the nucleation of perovskites in the solutions. This result indicates that the nucleation of perovskite and the solidification of polymer simultaneously occur and compete during the uniaxial electrospinning process. In striking contrast to this, the one-step coaxial electrospinning technique setup where the core and shell solutions were injected from separated needles can suppress the possible interactions between the perovskite precursors and PAN in the solution and enable the polymer to solidify first in the outer portion of the liquid jet during the electrospinning process so that the formed polymer shell can confine the perovskite solution in the core area to effectively restrict its crystal growth.

We further carried out the confocal fluorescence microscopy to image the luminescence

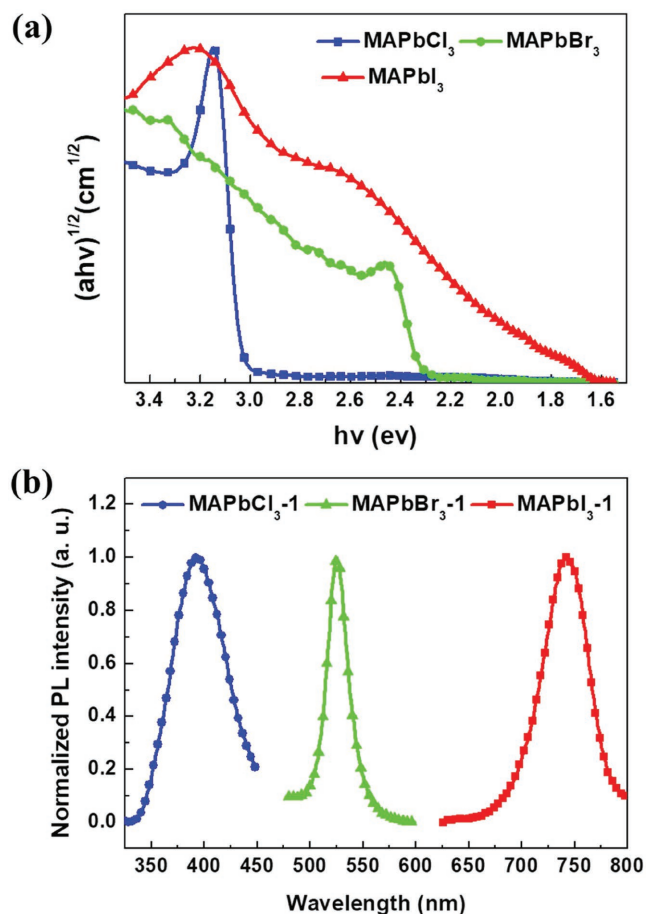


Figure 3. a) Tauc plot and b) photoluminescence spectra of MAPbCl₃-1, MAPbBr₃-1, and MAPbI₃-1 fibers.

of the perovskite nanocrystals in the electrospun fibers. As presented in Figure 2g–i, all the prepared electrospun fibers clearly show the homogeneous light emission, validating the effectiveness of coaxial electrospinning process to prepare perovskite nanofibers endowed with uniform distribution of nanocrystals inside them. By contrast, the nanofibers fabricated by uniaxial electrospinning process possess a nonuniform distribution of perovskite crystals and thus the discontinuous light emission as expected (Figure S1b, Supporting Information).

Figure 3 displayed the Tauc plot and PL spectra of the perovskite/PAN electrospun fibers and the relevant PL data can be found in Table 1. According to the onset of Kubelka–Munk-transformed diffuse reflectance spectrum (Figure 3a), the bandgaps of the MAPbCl₃-1, MAPbBr₃-1, and MAPbI₃-1 fibers are estimated to be 1.63, 2.32, and 3.04 eV, respectively. The maximum of their corresponding PL spectra are 394, 522, and 742 nm associated with the FWHM of 60.74, 27.66, and 51.77 nm, respectively (Figure 3b). Figure 4 portrayed the color-tunability of the prepared electrospun fiber via composition engineering. As shown, the color of the emitting light can be tuned by mixing bromide and iodide at different ratios in the perovskite composition. The PL spectrum of the MAPb(Br_xI_{1-x})₃ fibers was gradually blue-shifted from 711 to 550 nm as *x* increases from 0.2, 0.4, 0.6, to 0.8 (Table 1), affirming that the

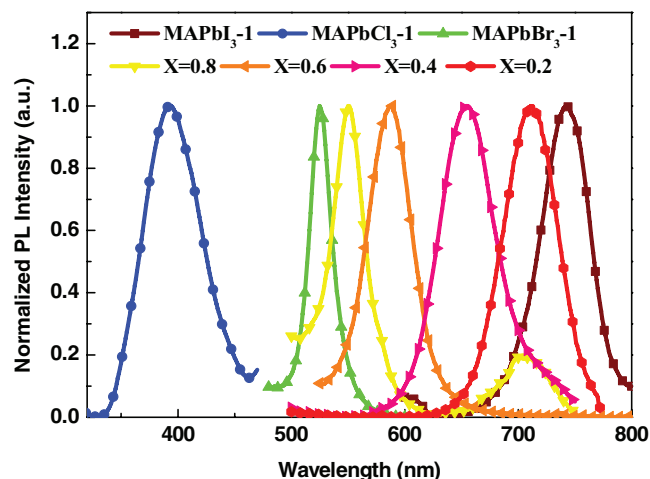


Figure 4. Photoluminescence spectra of the perovskite nanofibers. *x* is bromide fraction in the perovskites with mixed halides, MAPb(Br_{*x*}I_{1-*x*})₃.

colorful light-emitting perovskite/PAN electrospun fibers could be realized through the simple one-step coaxial electrospinning technique.

2.2. Effects of Precursor Stoichiometry and Polymer Concentration

It has been widely acknowledged that the composition of perovskite precursor plays a critical role on its resultant morphology and photophysical properties of perovskites.^[20,42] Considering the much faster crystallization of perovskite during the electrospinning process than the regular thin-film deposition, the stoichiometry of the precursor solution might even play a profound role. In this regard, we next fabricate the composite MAPbBr₃/PAN fibers using perovskite precursor solutions with different ratios of MABr:PbBr₂ (1.5:1 for MAPbBr₃-1 sample and 3:1 for MAPbBr₃-2 sample) and investigate their impacts on crystal size and luminous property of the prepared fiber. Furthermore, we also tune the concentration of the PAN solution to clarify the effect of the shell polymer, for which a diluted concentration of 60 from 100 mg mL⁻¹ is used to fabricate fibers. Besides, the corresponding MAPbBr₃/PAN spin-coated film (MAPbBr₃-film) was also prepared for a fair comparison.

Figure 5a–c shows the Tauc plot, PL spectra, and X-ray diffraction (XRD) data of the MAPbBr₃-1, MAPbBr₃-2, MAPbBr₃-3, and MAPbBr₃-film samples. We first discuss the effect of the stoichiometry of precursor solutions. As clearly shown, as increasing the MABr/PbBr₂ ratio from 1.5 (MAPbBr₃-1) to 3 (MAPbBr₃-2), the estimated bandgap of the prepared fiber was increased from 2.32 to 2.42 eV. Accordingly, the PL peak was slightly blue-shifted from 522 to 520 nm while the PLQY was increased from 21.9% to 24.8%, representing an enhancement of 13%. To understand the underlying reason for this enhancement, we further examine the crystallization of the perovskite nanostructures inside the fiber. As shown in Figure 5c, the XRD FWHM of the MAPbBr₃-2 sample estimated from the (100) peak at 2θ around 15° was slightly increased to 0.15° as compared to the value (0.14°) of MAPbBr₃-1 sample. It implies a decrease in the

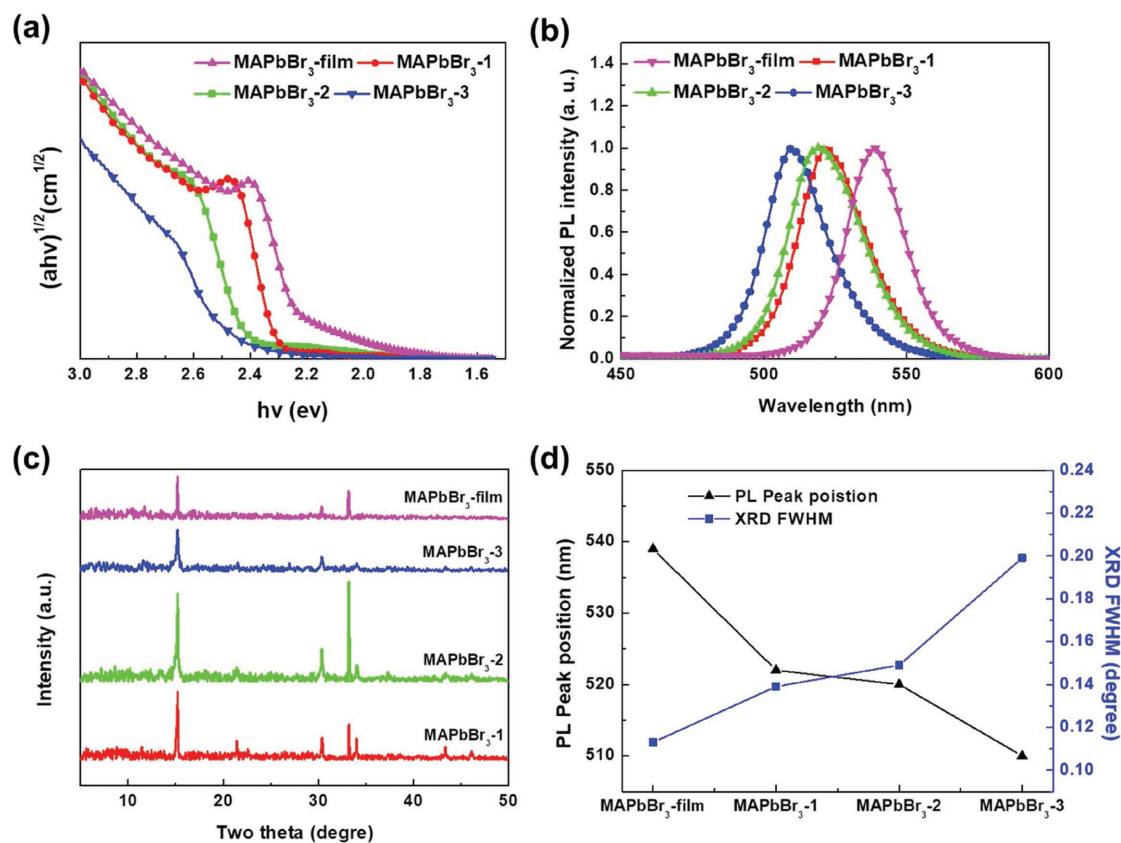


Figure 5. a) Tauc plot, b) photoluminescence spectra, and c) XRD data of MAPbBr₃-1 fiber, MAPbBr₃-2 fiber, MAPbBr₃-3 fiber, and MAPbBr₃-film. d) PL peak position and XRD FWHM of the (100) peak of the studied samples.

crystal size as the MABr/PbBr₂ ratio increases, which is well consistent with the grain sizes observed in the TEM images (Figure S3, Supporting Information), in which an average size of 26.89 ± 6.96 and 12.54 ± 6.06 nm could be found for the MAPbBr₃-1 and MAPbBr₃-2 fibers, respectively. This result therefore indicates that the excess MABr might retard the crystal growth of perovskite to result in the smaller crystals, thus yielding a higher PLQY due to the stronger geometrical confinement effects.

Afterward, we investigate the effect of PAN concentration by comparing MAPbBr₃-2 and MAPbBr₃-3 fibers. It is revealed that the fiber diameter was greatly decreased from 541 ± 89 to 194 ± 16 nm as the concentration of PAN solutions in the shell site is diluted from 100 to 60 mg mL⁻¹. Similar to the effect of increasing MABr/PbBr₂ precursor ratio, the corresponding onset in the Tauc plot was blue-shifted from 2.42 to 2.44 eV and the PL signal was blue-shifted from 520 to 510 nm. Notably, the PLQY of MAPbBr₃-3 is further enhanced to 30.9%, showing a 25% enhancement as compared to the MAPbBr₃-2 fiber. Similarly, the XRD FWHM of the (100) peak of MAPbBr₃-3 fiber was observed to increase from 0.15° (MAPbBr₃-2 fiber) to 0.20°, suggesting a decrease in the grain size. It is also evident in its corresponding TEM image (Table 1; Figure S3, Supporting Information), wherein an average grain size of 8.58 ± 2.32 nm was observed. This result suggests that using a lower PAN concentration to prepare the polymeric shell can afford the formation of perovskite nanocrystals with smaller size. This

could be attributed to the faster solvent evaporation rate of the core perovskite solution provided the thinner PAN shell layer formed at a lower concentration during the electrospinning process, which in turn shortens the perovskite crystallization time and ends up with smaller crystals sizes to be confined in the thinner fibers.

As a point of note, the differences between the regular perovskite film and our prepared electrospun fiber can be investigated by comparing MAPbBr₃-3 and MAPbBr₃-film samples. First, it can be observed that the grain size of the perovskite crystals in MAPbBr₃-film is much larger with an average size of 0.97 ± 0.27 μm as determined by its corresponding SEM image (Figure S2a, Supporting Information) and the small XRD FWHM ($\approx 0.11^\circ$) of the (100) peak. As shown in Figure 5a, the estimated bandgap of MAPbBr₃-film was ≈ 2.23 eV, which is much lower than that of MAPbBr₃-3 fiber (2.44 eV). Also, the peak PL of MAPbBr₃-3-film is located at 540 nm, which is 29-nm-red-shifted as compared to MAPbBr₃-3 fiber. However, the MAPbBr₃-3 fiber delivers a much higher PLQY of 30.9% as compared to the MAPbBr₃-film, which only yield a moderate PLQY of 6.8%. Besides, it is interesting to note that all the MAPbBr₃-based electrospun fibers demonstrate higher PLQY to its thin-film counterpart (Table 1). Such superior PL characteristics of the electrospun fibers are benefited from the geometric confinement effect as discussed earlier, for which the small grain size of the perovskite nanocrystals embedded in the fibers dominates the enhancement. In this regard, it can

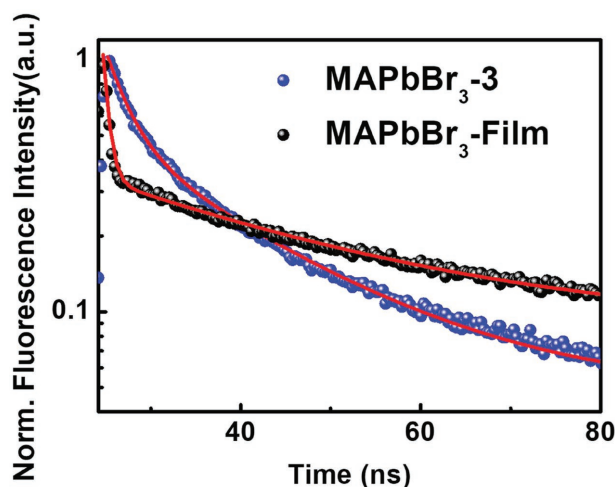


Figure 6. Time-resolved PL spectra of MAPbBr₃-3 ($\tau_1 = 2.03$ ns, $\tau_2 = 13.37$ ns) and MAPbBr₃-film ($\tau_1 = 0.41$ ns, $\tau_2 = 19.35$ ns).

be concluded that the fast evaporation of solvent during electrospinning process as well as the in situ formation of confined perovskites nanocrystals by coaxial electrospinning technique is an effective approach to prepare perovskite fibers with promising luminescent properties.

Figure 5d summarized the PL peak positions and XRD FWHMs for the studied samples. As shown, the PL peak of the perovskite-based fiber is blue-shifted compared to that of reference thin film. For the fibers, while the ratio of MABr/PbBr₂ increases and the shell PAN concentration decreases, the resultant PL peak is further blue-shifted, concomitant with an increase in XRD FWHM as a result of decreased crystal size. The results clearly highlight the importance of stoichiometry of perovskite precursors and the concentration of shell polymer used for the coaxial electrospinning process, which greatly impacts the resulting sizes of perovskite crystals and the luminescent properties.

To better understand the charge dynamics of our prepared fibers, the time-resolved photoluminescence spectra were measured as shown in Figure 6. In order to exclude the influence from moisture and air, a thin poly(methyl methacrylate) film was spin-coated onto the samples before testing. The PL decay was fitted using the following equation considering a short-lived PL lifetime (τ_1) and a long-lived PL lifetime (τ_2).

$$A(t) = A_1 \exp\left(\frac{-t}{\tau_1}\right) + A_2 \exp\left(\frac{-t}{\tau_2}\right) \quad (1)$$

It has been reported that the short-lived PL lifetime (τ_1) correlates with the trapping of excitons by crystal defects, i.e., a nonradiative trapping process. As shown, the estimated τ_1 of MAPbBr₃-3 fiber is ≈ 2.03 ns, which is higher than the value (0.41 ns) of the MAPbBr₃-film, suggesting the less nonradiative recombination occurring in MAPbBr₃-3. On the other hand, the long-lived component (τ_2) is dependent on the crystal size, for which a smaller size of perovskite grains will incur a greater probability of exciton recombination. As seen, the MAPbBr₃-3 fiber showed a much shorter τ_2 of 13.37 ns as compared to the value (19.35 ns) of the MAPbBr₃-film, indicating a

more efficient radiative recombination in the fiber. This result reveals that the MAPbBr₃-3 fiber possesses less defects and its smaller grain size than the MAPbBr₃-film provides conspicuous geometric confinement effect to boost the PL emission and QY.

2.3. Stability and Waterproof Tests

The perovskite has been documented to be sensitive to moisture and air.^[43] However, for the fibers prepared by the coaxial electrospinning technique, the perovskite crystals are well confined inside the fibers, wherein the outer shell polymer can prevent the core perovskites from moisture. In this respect, we tested the long-term stability of MAPbBr₃-3 fiber in atmosphere and in water in parallel with the reference MAPbBr₃-film to verify the improved stability of our prepared fibers. As shown in Figure 7a, the MAPbBr₃-3 fibrous mat is very stable under the atmospheric environment. Its initial PL intensity is almost remained for at least one month while stored at 28 °C with a relative humidity of 80%. In contrast, the intensity of MAPbBr₃-film drops decisively (inserted in Figure 7a). Its initial PL intensity decays over 50% in the first 10 h and <20% remaining after 40 h which may be resulted from the exposure of perovskite crystals on the surface of MAPbBr₃-film as shown in Figure S2a in the Supporting Information.

In order to test the waterproof ability, the studied samples were directly immersed in water and the time-dependent PL intensities of the samples are tracked as shown in Figure 7b. As seen, the PL intensity of the MAPbBr₃-3 fiber can maintain $\approx 50\%$ of its initial value after 48-h immersion. In a striking contrast, the PL intensity of the MAPbBr₃-film sample rapidly decays to 20% of its initial value within 15 s and to 0% in 10 min (see the inset in Figure 7b). Figure 7c displayed the authentic photographs of the MAPbBr₃-3 fibrous mats after immersion in water for different period of time, wherein the green color emitted from the mat can still be clearly seen even after 120-h immersion. Apparently, it is attributed to protection from the shell polymer that shields the perovskites from water. For the MAPbBr₃-3 fibrous mats, the PAN can completely cover the core perovskite nanocrystals whereas it cannot completely cover the MAPbBr₃-film, as exemplified by the SEM image shown in Figure S2 in the Supporting Information.

2.4. White Light Emitting Fiber

Hai et al. have recently reported that the multinozzle electrospinning can be used to mix three color CsPbX₃ quantum dots in the fibrous mats to emit white light.^[33] As inspired by this study, we aim to develop white light-emitting fibers prepared by our simple one-step coaxial electrospinning technique without the need for presynthesis of perovskite quantum dots. In Figure 4, we have shown that the mixed halide perovskite fiber, MAPb(Br_{0.6}I_{0.4})₃, possesses a maximum PL intensity peak at 589 nm. Herein, we rationally use this mixed halide perovskite as the core material and a blue light-emitting conjugated polymer, PFN, which is mixed with PAN as the shell material to prepare the white light-emitting electrospun nanofibers.

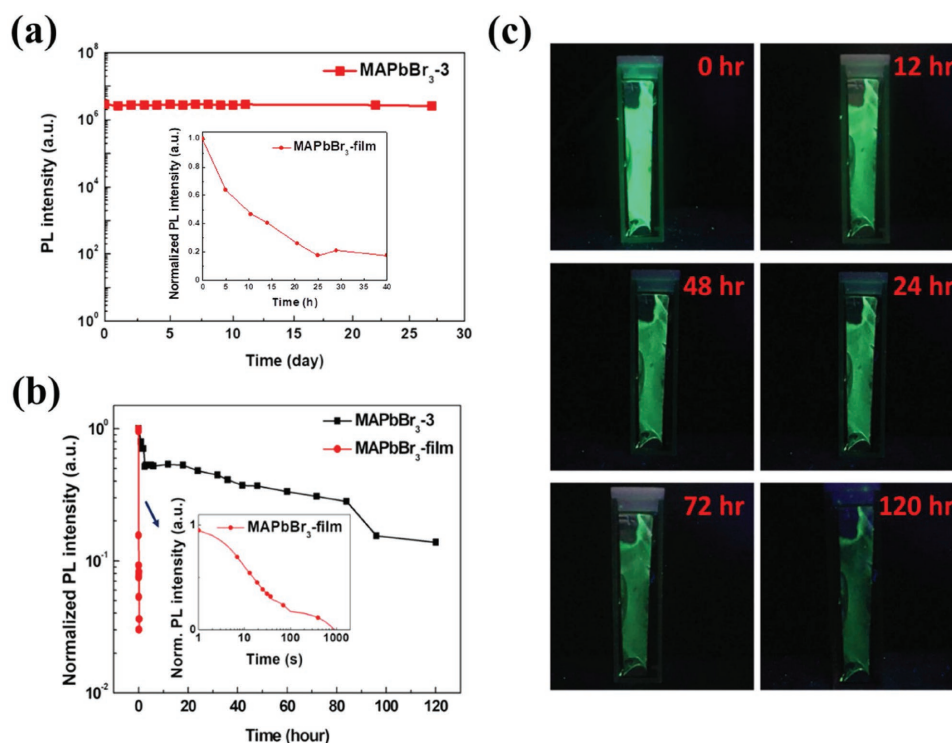


Figure 7. a) Stability test of MAPbBr₃-3 fibrous mat and MAPbBr₃-film at 28 °C and 80% humidity, b) waterproof test of MAPbBr₃-3 fibrous mat and MAPbBr₃-film soaked in water, and c) photographs of immersed MAPbBr₃-3 fibrous mat in water for different period of time.

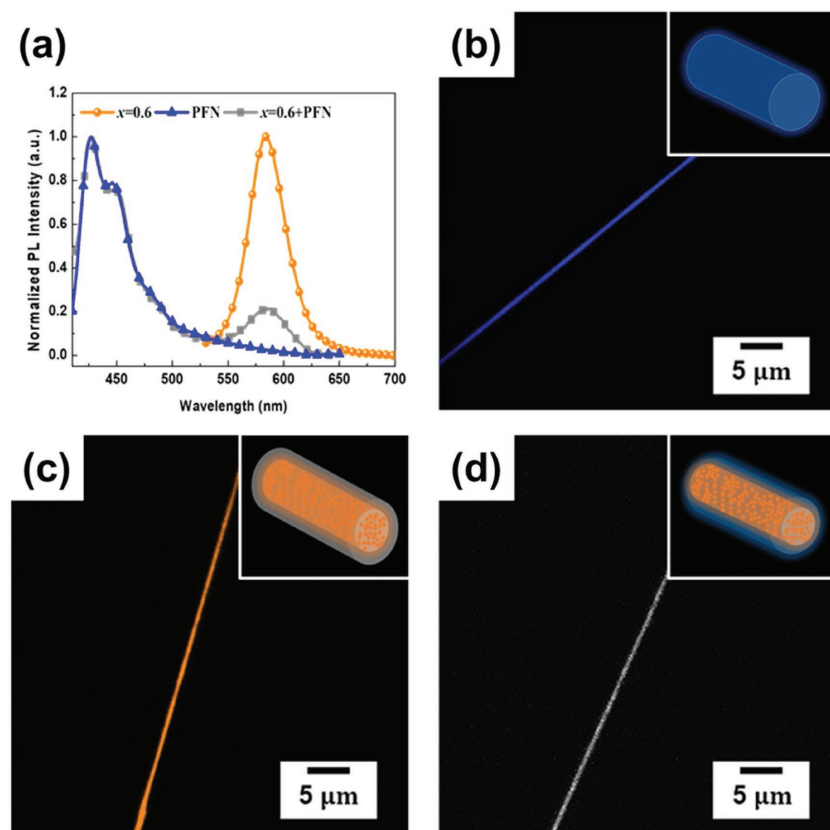


Figure 8. a) PL spectra of simplex PFN, MAPb(Br_{0.6}I_{0.4})₃, and MAPb(Br_{0.6}I_{0.4})₃/PFN fibers and the confocal images of b) PFN, c) MAPb(Br_{0.6}I_{0.4})₃, and d) MAPb(Br_{0.6}I_{0.4})₃/PFN fibers.

Figure 8a compares the PL spectra of simplex PFN, MAPb(Br_{0.6}I_{0.4})₃, and MAPb(Br_{0.6}I_{0.4})₃/PFN fibers, wherein the MAPb(Br_{0.6}I_{0.4})₃/PFN fiber exhibits exactly the PL characteristics from both components. Their corresponding confocal images are shown in Figure 8b,c, where continuous light emission along the fibers can be clearly observed. The chromaticities of these three fibers were found to lie within the blue, orange, and white region, respectively and their commensurate commission internationale de l'éclairage chromaticity diagrams are illustrated in Figure S4 in the Supporting Information. This result demonstrates that by simply tuning the ratio of halides in the core precursor solutions and simultaneously incorporating appropriate organic conjugated materials in the shell polymer, white light-emitting fibers can be achieved by the facile one-step coaxial electrospinning technique.

3. Conclusion

In summary, we herein, for the first time, exploited the one-step coaxial electrospinning technique to fabricate the uniform luminous perovskite nanofibers. The coaxial electrospinning technique involves the core/shell

technique, for which the perovskite precursor solution was employed in the core site while the polymer solution was used in the outer shell site. We not only demonstrated the color-tunability of the emitting light can be obtained by tuning the halide (Cl, Br, and I) composition of perovskite but also revealed that the stoichiometry of the perovskite precursors and the concentration of the polymer solutions largely affected the grain size of the perovskite nanocrystals. As a result, the optimized perovskite electrospun fiber could yield a high PLQY of 30.9%, surpassing the value of its thin-film counterpart. Moreover, owing to the hydrophobic nature of the shell polymer, the prepared perovskite fiber was endowed with a high ambient stability and a high resistance to water. We manifested that a strong PL intensity of the fibers could still be tracked even immersed in water for 120 h. Finally, a white light-emitting electrospun nanofiber was successfully prepared by pairing the orange light-emitting compositional perovskite in the core site with a blue light-emitting conjugated polymer in the shell site. This work unveils the potential of coaxial electrospinning technique to fabricate efficient light-emitting perovskite nanofibers.

4. Experimental Section

Materials: PAN ($M_w \approx 150\,000$) was used as received from Sigma-Aldrich. The lead halide compounds with $\geq 98\%$ purity (PbX_2 , $X = Cl, Br, I$) were purchased from Alfa Aesar. *N, N*-Dimethylformamide (DMF, anhydrous $\geq 99\%$), dimethyl sulfoxide (DMSO, anhydrous, $\geq 99\%$), and MAX ($X = Cl, Br, I$) were purchased from Sigma-Aldrich. All chemicals were used without further purification. PFN ($M_w > 10\,000$) was purchased from Luminescence Technology Corp.

Preparation of Core and Shell Solutions: The precursors, PbX_2 and MAX, for $MAPbBr_3$ and $MAPbI_3$ were dissolved in DMF while the precursors for $MAPbCl_3$ were dissolved in DMSO:DMF = 1:1 cosolvent because of the low solubility of the chloride precursors in pure DMF. The molar ratios of the precursors (MAX/ PbX_2) in the solutions for all the samples are listed in Table 1 and the overall precursor concentration was 2.5 m. For the samples of mixed halides, $MAPb(Br_xI_{1-x})_3$, the precursors of $MABr:PbBr_2$ and $MAI:PbI_2$ at 1.5:1 were first dissolved in DMF and were then mixed at the desired ratios ($x = 0.2, 0.4, 0.6, 0.8$). The shell solutions were prepared by dissolving 500 or 300 mg PAN in 5 mL DMF (100 or 60 mg mL⁻¹). In preparation of the white light-emitting nanofibers, 500 mg PAN and 25 mg PFN were dissolved in 5 mL DMF and then 75 μ L acetic acid was added into the solution to enhance the solubility of PFN.

Preparation of Electrospun Fibers and Thin Films: A two-fluid coaxial electrospinning process was used to fabricate the core-shell nanofibers, similar to the previous reports.^[23,24,30,44] Figure 1 shows the schematic of the experimental setup. Two syringes were used and each syringe was connected to a separate needle, for which one needle with diameter of 0.90 mm was placed inside the other with diameter of 1.25 mm to form the two-fluid coaxial electrospinning system with the perovskite precursor solution in the core and the polymer solution in the shell. The two solutions were continuously fed into the coaxial capillaries by two syringe pumps (KD Scientific Model 100, USA). The flow rate of the core and shell solutions were 0.1 and 1 mL h⁻¹ for the shell polymer concentration at 100 mg mL⁻¹, while the flow rate of the core and shell solutions were 0.06 and 0.6 mL h⁻¹ for the shell concentration at 60 mg mL⁻¹. The tip of the core needle was connected to a high-voltage power supply (chargemaster CH30P SIMCO, USA). The voltage was set at 12.9 kV and the working distance (the distance between the tip of the needle and collector) was 20 cm for collecting the nonwoven nanofibers. The electrospinning process was operated at 25 °C and 50% relative humidity, and kept in stable cone-jet spinning mode monitored

by a charge coupled device (CCD) camera (Xli 3M USB2.0 CCD camera, USA) and Macro video zoom lens (OPTEM MVZL, USA) to ensure the uniformity of nanofibers. Thin film samples were prepared by mixing PAN and precursors in DMF and the solutions were spin-coated into films at 1000 rpm for 60 s. The concentration of PAN is 60 mg mL⁻¹ and the precursor molar ratio MABr:PbBr₂ is 3:1. All of the collected fibers and thin films were placed in vacuum oven overnight before characterization.

Characterization: SEM images were taken with JEOL JSM-6330F at an accelerating voltage of 10 kV. Before imaging, the samples were sputtered with Pt. TEM images were taken with FEI Tecnai G2 20 operated at 200 keV. Fluorescence optical microscope images were taken by a two photon laser confocal microscope (Leica LCS SP5). UV-vis absorption spectra were recorded using Hitachi U-4100 spectrophotometer. Steady-state PL and time-resolved photoluminescence were recorded by the Spex Fluorolog-3 spectrofluorometer system (Horiba Jobin Yvon). Crystal structures of perovskites in nanofibers were investigated by Rigaku-UltimaIV X-Ray diffractometer with Cu K α radiation ($\lambda = 1.5418 \text{ \AA}$).

Supporting Information

Supporting Information is available from the Wiley Online Library or from the author.

Acknowledgements

The financial support from National Science Council of Taiwan, Ministry of Economics Affairs of Taiwan, and National Taiwan University Excellent Research program are highly appreciated. Besides, the authors also gratefully acknowledge the Instrumentation Center (sponsored by National Science Council, Taiwan) for the Cold-field emission Scanning Electron Microscope (Hitachi S-4800) and Technology Commons in College of Life Science, National Taiwan University for the confocal experiment.

Conflict of Interest

The authors declare no conflict of interest.

Keywords

core-shell, electrospun nanofibers, geometric confinement, light emission, perovskite

Received: December 16, 2017

Revised: February 26, 2018

Published online: April 30, 2018

- [1] Y. Sun, Y. Wu, X. Fang, L. Xu, Z. Ma, Y. Lu, W.-H. Zhang, Q. Yu, N. Yuan, J. Ding, *J. Mater. Chem. A* **2017**, 5, 1374.
- [2] H. Cho, S.-H. Jeong, M.-H. Park, Y.-H. Kim, C. Wolf, C.-L. Lee, J. H. Heo, A. Sadhanala, N. Myoung, S. Yoo, *Science* **2015**, 350, 1222.
- [3] L. Dou, Y. M. Yang, J. You, Z. Hong, W.-H. Chang, G. Li, Y. Yang, *Nat. Commun.* **2014**, 5, 5404.
- [4] J. Y. Chen, Y. C. Chiu, Y. T. Li, C. C. Chueh, W. C. Chen, *Adv. Mater.* **2017**, 29, 1702217.
- [5] K. Yang, F. Li, C. P. Veeramalai, T. Guo, *Appl. Phys. Lett.* **2017**, 110, 083102.

- [6] E. Ercan, J.-Y. Chen, P.-C. Tsai, J.-Y. Lam, S. C.-W. Huang, C.-C. Chueh, W.-C. Chen, *Adv. Electron. Mater.* **2017**, *3*, 1700344.
- [7] S. A. Veldhuis, P. P. Boix, N. Yantara, M. Li, T. C. Sum, N. Mathews, S. G. Mhaisalkar, *Adv. Mater.* **2016**, *28*, 6804.
- [8] X. Y. Chin, D. Cortecchia, J. Yin, A. Bruno, C. Soci, *Nat. Commun.* **2015**, *6*, 7383.
- [9] F. Maddalena, X. Y. Chin, D. Cortecchia, A. Bruno, C. Soci, presented at *2017 Conf. on Lasers and Electro-Optics Europe & European Quantum Electronics Conf. (CLEO/Europe-EQEC)*, Munich, Germany, June **2017**.
- [10] H. Kim, J. S. Han, J. Choi, S. Y. Kim, H. W. Jang, *Small Methods* **2018**, *2*, 1700310.
- [11] S. Bai, Z. Yuan, F. Gao, *J. Mater. Chem. C* **2016**, *4*, 3898.
- [12] S. Gonzalez-Carrero, R. E. Galian, J. Pérez-Prieto, *J. Mater. Chem. A* **2015**, *3*, 9187.
- [13] H. Huang, L. Polavarapu, J. A. Sichert, A. S. Susha, A. S. Urban, A. L. Rogach, *NPG Asia Mater.* **2016**, *8*, e328.
- [14] B. Ortaç, F. Kayaci, H. A. Vural, A. E. Deniz, T. Uyar, *React. Funct. Polym.* **2013**, *73*, 1262.
- [15] Y. H. Kim, H. Cho, T. W. Lee, *Proc. Natl. Acad. Sci. USA* **2016**, *113*, 11694.
- [16] W. Zhang, G. E. Eperon, H. J. Snaith, *Nat. Energy* **2016**, *1*, 16048.
- [17] Z. K. Tan, R. S. Moghaddam, M. L. Lai, P. Docampo, R. Higler, F. Deschler, M. Price, A. Sadhanala, L. M. Pazos, D. Credgington, F. Hanusch, T. Bein, H. J. Snaith, R. H. Friend, *Nat. Nanotechnol.* **2014**, *9*, 687.
- [18] S. Demchyshyn, J. M. Roemer, H. Grois, H. Heilbrunner, C. Ulbricht, D. Apaydin, A. Bohm, U. Rutt, F. Bertram, G. Hesser, M. C. Scharber, N. S. Sariciftci, B. Nickel, S. Bauer, E. D. Głowacki, M. Kaltenbrunner, *Sci. Adv.* **2017**, *3*, e1700738.
- [19] J. Yan, B. Zhang, Y. Chen, A. Zhang, X. Ke, *ACS Appl. Mater. Interfaces* **2016**, *8*, 12756.
- [20] J. W. Lee, Y. J. Choi, J. M. Yang, S. Ham, S. K. Jeon, J. Y. Lee, Y. H. Song, E. K. Ji, D. H. Yoon, S. Seo, H. Shin, G. S. Han, H. S. Jung, D. Kim, N. G. Park, *ACS Nano* **2017**, *11*, 3311.
- [21] F. Zhang, H. Zhong, C. Chen, X.-G. Wu, X. Hu, H. Huang, J. Han, B. Zou, Y. Dong, *ACS Nano* **2015**, *9*, 4533.
- [22] D. Li, Y. Xia, *Adv. Mater.* **2004**, *16*, 1151.
- [23] J.-Y. Chen, H.-C. Wu, Y.-C. Chiu, W.-C. Chen, *Adv. Energy Mater.* **2014**, *4*, 1301665.
- [24] H. C. Chang, C. L. Liu, W. C. Chen, *Adv. Funct. Mater.* **2013**, *23*, 4960.
- [25] J.-Y. Chen, C.-C. Kuo, C.-S. Lai, W.-C. Chen, H.-L. Chen, *Macromolecules* **2011**, *44*, 2883.
- [26] C.-C. Kuo, C.-T. Wang, W.-C. Chen, *Macromol. Mater. Eng.* **2008**, *293*, 999.
- [27] J. Song, M. Chen, M. B. Olesen, C. Wang, R. Havelund, Q. Li, E. Xie, R. Yang, P. Boggild, C. Wang, F. Besenbacher, M. Dong, *Nanoscale* **2011**, *3*, 4966.
- [28] P. Wang, L. Zhang, Y. Xia, L. Tong, X. Xu, Y. Ying, *Nano Lett.* **2012**, *12*, 3145.
- [29] J.-Y. Chen, Y.-C. Chiu, C.-C. Shih, W.-C. Wu, W.-C. Chen, *J. Mater. Chem. A* **2015**, *3*, 15039.
- [30] D. Li, Y. Wang, Y. Xia, *Nano Lett.* **2003**, *3*, 1167.
- [31] H. Jeong, J. K. Lee, *ACS Appl. Mater. Interfaces* **2015**, *7*, 28459.
- [32] D. Li, Y. Wang, Y. Xia, *Adv. Mater.* **2004**, *16*, 361.
- [33] J. Hai, H. Li, Y. Zhao, F. Chen, Y. Peng, B. Wang, *Chem. Commun.* **2017**, *53*, 5400.
- [34] Y. Wang, Y. Zhu, J. Huang, J. Cai, J. Zhu, X. Yang, J. Shen, H. Jiang, C. Li, *J. Phys. Chem. Lett.* **2016**, *7*, 4253.
- [35] Y. Wang, Y. Zhu, J. Huang, J. Cai, J. Zhu, X. Yang, J. Shen, C. Li, *Nanoscale Horiz.* **2017**, *2*, 225.
- [36] Y.-W. Lin, C.-J. Lin, Y.-H. Chou, C.-L. Liu, H.-C. Chang, W.-C. Chen, *J. Mater. Chem. C* **2013**, *1*, 5336.
- [37] R. Rivera, R. Kappera, M. Sin, M. Chhowalla, A. Safari, presented at *2014 Joint IEEE Int. Symp. on the Applications of Ferroelectric, Int. Workshop on Acoustic Transduction Materials and Devices & Workshop on Piezoresponse Force Microscopy*, PA, USA, May **2014**.
- [38] Q. Chen, N. De Marco, Y. M. Yang, T.-B. Song, C.-C. Chen, H. Zhao, Z. Hong, H. Zhou, Y. Yang, *Nano Today* **2015**, *10*, 355.
- [39] G. Niu, X. Guo, L. Wang, *J. Mater. Chem. A* **2015**, *3*, 8970.
- [40] Y. Fu, F. Meng, M. B. Rowley, B. J. Thompson, M. J. Shearer, D. Ma, R. J. Hamers, J. C. Wright, S. Jin, *J. Am. Chem. Soc.* **2015**, *137*, 5810.
- [41] T. Ou, J. Yan, C. Xiao, W. Shen, C. Liu, X. Liu, Y. Han, Y. Ma, C. Gao, *Nanoscale* **2016**, *8*, 11426.
- [42] V. D'Innocenzo, A. R. Srimath Kandada, M. De Bastiani, M. Gandini, A. Petrozza, *J. Am. Chem. Soc.* **2014**, *136*, 17730.
- [43] R. Sheng, X. Wen, S. Huang, X. Hao, S. Chen, Y. Jiang, X. Deng, M. A. Green, A. W. Ho-Baillie, *Nanoscale* **2016**, *8*, 1926.
- [44] A. Babel, D. Li, Y. N. Xia, S. A. Jenekhe, *Macromolecules* **2005**, *38*, 4705.